Interaction of precipitation with austenite-to-ferrite phase transformation in vanadium micro-alloyed steels

Ioannidou, Chrysoula; Arechabaleta Guenechea, Zaloa; Navarro Lopez, Alfonso; Rijkenberg, Arjan; Dalgliesh, Robert M.; Kölling, Sebastian; Bliznuk, Vitaliy; Pappas, Catherine; Sietsma, Jilt; van Well, Ad

DOI
10.1016/j.actamat.2019.09.046

Publication date
2019

Document Version
Final published version

Published in
Acta Materialia

Acta Materialia 181 (2019) 10–24

Contents lists available at ScienceDirect

Acta Materialia

journal homepage: www.elsevier.com/locate/actamat

Full length article

Interaction of precipitation with austenite-to-ferrite phase transformation in vanadium micro-alloyed steels

Chrysoula Ioannidou[a,*], Zaloa Arechabaleta[a,1], Alfonso Navarro-López[a], Arjan Rijkenberg[b], Robert M. Dalgliesh[c], Sebastian Kölling[d], Vitaliy Bliznuk[e], Catherine Pappas[f], Jilt Sietsma[a], Ad A. van Well[f], S. Erik Offerman[a]

[a] Department of Materials Science and Engineering, Delft University of Technology, Mekelweg 2, 2628 CD Delft, the Netherlands
[b] Tata Steel Europe, 1970 CA IJmuiden, the Netherlands
[c] STFC, ISIS, Rutherford Appleton Laboratory, Chilton, Oxfordshire, OX11 0QX, United Kingdom
[d] Department of Applied Physics, Eindhoven University of Technology, PO Box 513, 5600 MB Eindhoven, the Netherlands
[e] Department of Electrical Energy, Metals, Mechanical Constructions and Systems, Ghent University, Tech Lane Ghent Science Park – Campus A, Technologiepark 903, 9052 Zwijnaarde, Ghent, Belgium
[f] Department of Radiation Science and Technology, Faculty of Applied Sciences, Delft University of Technology, Mekelweg 15, 2629 JB Delft, the Netherlands

ARTICLE INFO

Article history:
Received 13 June 2019
Revised 23 September 2019
Accepted 23 September 2019
Available online 26 September 2019

Keywords:
Micro-alloyed steel
Vanadium carbide interphase precipitation
Austenite-to-ferrite phase transformation kinetics
Small-angle neutron scattering
Atom Probe Tomography

ABSTRACT

The precipitation kinetics of vanadium carbides and its interaction with the austenite-to-ferrite phase transformation is studied in two micro-alloyed steels that differ in vanadium and carbon concentrations by a factor of two, but have the same vanadium-to-carbon atomic ratio of 1:1. Dilatometry is used for heat-treating the specimens and studying the phase transformation kinetics during annealing at isothermal holding temperatures of 900, 750 and 650 °C for up to 10 h. Small-Angle Neutron Scattering (SANS) and Atom Probe Tomography (APT) measurements are performed to study the vanadium carbide precipitation kinetics. Vanadium carbide precipitation is not observed after annealing for 10 h at 900 and 750 °C, which is contrary to predictions from thermodynamic equilibrium calculations. Vanadium carbide precipitation is only observed during or after the austenite-to-ferrite phase transformation at 650 °C. The precipitate volume fraction and mean radius continuously increase as holding time increases, while the precipitate number density starts to decrease after 20 min, which corresponds to the time at which the austenite-to-ferrite phase transformation is finished. This indicates that nucleation and growth are dominant during the first 20 min, while later precipitate growth with soft impingement (overlapping diffusion fields) and coarsening take place. APT shows gradual changes in the precipitate chemical composition during annealing at 650 °C, which finally reaches a 1:1 atomic ratio of vanadium-to-carbon in the core of the precipitates after 10 h.

1. Introduction

The improvement of fuel economy, the reduction of CO_2 emission, and the fulfilment of European Union initiatives [1] and legislations [2] are key drivers for the automotive industry nowadays to reduce the vehicle weight. This includes weight reduction in the chassis and suspension system, which requires that steel offers high strength, ductility and stretch flange-ability for the manufacturing of intricate and complex light-weight components. Micro-alloyed steels containing nano-sized precipitates in a ferrite matrix are promising candidates to meet these requirements simultaneously [3–6] and are already used in chassis and suspension parts [3,4,7–9]. However, these alloys contain a considerable amount of micro-alloying additions [6]. Based on the above demands, resource-efficient steels, which contain smaller amounts of micro-alloying elements and critical raw materials [10] while maintaining their good mechanical properties, are of great interest.

Titanium (Ti), niobium (Nb), molybdenum (Mo) and vanadium (V) are widely used as micro-alloying elements to improve the performance of steel through their effect on the microstructure and consequently on the mechanical properties [3–6,11–22]. These elements contribute to grain size refinement, recrystallization retardation and precipitate formation. The focus of the present work is on vanadium, which is well known for providing precipitation strengthening to steels and which has, therefore, attracted a lot of

* Corresponding author.
E-mail address: c.ioannidou@tudelft.nl (C. Ioannidou).
[1] Present address: Tecnalia Research & Innovation, Geldo, Building 700, 48160 Derio, Spain.

https://doi.org/10.1016/j.actamat.2019.09.046
1359-6454/

interest in the last decades [4,6,13,15–20,23,24]. Vanadium carbide (VC) precipitation can take place in the migrating austenite/ferrite interface during the austenite-to-ferrite phase transformation, i.e. interphase precipitation, and in ferrite. The solubility of the vanadium carbides in austenite is high, higher than the solubility of the carbides of Ti and Nb, and therefore vanadium carbides do not tend to form in austenite. However, due to the solubility drop of vanadium carbide when austenite transforms to ferrite, interphase precipitation as well as precipitation in ferrite are favoured [15]. This reduces the rate of precipitate coarsening and leads to a fine precipitate distribution, which is critical for the hardening of the steel [15]. Due to the beneficial contribution of the vanadium carbides to the overall mechanical properties of steel and the necessity to make optimum use of vanadium, more research is required to understand the vanadium carbide precipitation and its interaction with the austenite-to-ferrite phase transformation.

Extensive research has been carried out on vanadium carbides and it is found that the precipitates' characteristics and kinetics are strongly dependent on the steel composition and treatment conditions. The transformation temperature and time are critical factors for the precipitation, determining the type of precipitation (interphase or random) and the precipitate size, shape, composition, number density and volume fraction [15–29] . The vanadium carbide crystal structure is observed to be of the NaCl-type of stoichiometric VC [16,24], $VC_{0.9}$ [20], V_4C_3 [13,27], or V_6C_5 [28], in a range of transformation temperatures from 600 to 700 °C. The vanadium carbide precipitates have a Baker Nutting orientation relationship with the BCC ferrite matrix [16,30], while their nucleation is favourable at non-Kurdjumov-Sachs ferrite/austenite interfaces [31,32]. Their shape can be spherical [13,17–19,23,24], disk-like [13,20,24], ellipsoidal [19,20], rod-like [13], needle-like or cuboid [27], depending on the conditions described above. Furthermore, different levels of alloying elements (like Mo, Ti, Nb and N) are found to affect the vanadium carbide precipitates composition [13,15,16], shape [13,27] and preferable growth direction [13,15,16,27]. For instance, in ref. [13], in low-carbon steels containing vanadium and molybdenum, the latter is present in the precipitates, forming disk-shaped (V,Mo)C growing along the (001) ferrite plane, and rod-shaped $(V,Mo)_4C_3$ growing along the (011) ferrite plane.

Transmission Electron Microscopy (TEM) and Atom Probe Tomography are mainly used for the precipitates characterization [12–14,17–21,23–28,31–34]. Detailed research on vanadium carbide precipitation in low-Carbon steels has been done by Kamikawa et al. [19] and Zhang et al. [26,29], who have extensively measured the precipitate size distribution and number density and their effect on the mechanical properties of the steel as a function of temperature and for various steel compositions. However, scarce literature on the kinetics of the precipitation is reported. Moreover, APT and TEM are limited in providing accurate statistical information on precipitate size distribution, number density and volume fraction, since the measured sample volume is usually relatively small (in the order of $\sim 10^6$ nm^3).

Small-Angle Neutron Scattering delivers statistical information regarding the average size, volume fraction, number density and size distribution of precipitates over larger specimen volumes [35] (e.g. $10 \times 10 \times 1\ mm^3$). Previous SANS studies have been performed on Ti-Mo micro-alloyed steel [14], NbC precipitates in austenite [22] and in ferrite [36], Fe-Cu alloys [37], Fe-Au alloys [38], maraging steels [39] and low-carbon steels [40]. SANS measurements on low-carbon V-micro-alloyed steels have only recently been reported [20,23,24]. The precipitation kinetics of disk-shaped and oblate vanadium carbides at 700 °C in a low-carbon steel [20], and of spherical and disk-shaped vanadium carbides in a temperature range from 600 to 700 °C in a medium-carbon steel, has been characterised by SANS at room temperature [24].

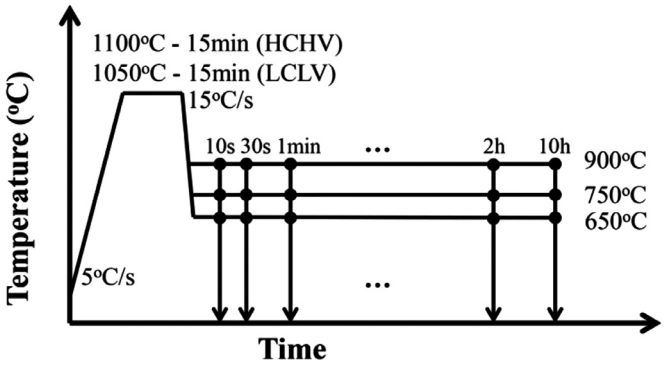

Fig. 1. Schematic representation of the thermal cycles applied in the dilatometer.

The present study aims to provide *quantitative* information on the vanadium carbide precipitation *kinetics* in low-Carbon steels differing in vanadium and carbon content and heat treated at different temperatures (900, 750 and 650 °C) than previously reported in the literature. Emphasis is given on the *kinetics* of precipitation for up to 10 h of annealing, on the interaction of the precipitation kinetics with the austenite-to-ferrite phase transformation kinetics and on the time *evolution of the precipitate chemical composition* during annealing. Small-Angle Neutron Scattering is combined with dilatometry, Atom Probe Tomography and Transmission Electron Microscopy for a comprehensive study of the precipitation and phase transformation kinetics.

2. Experimental

Two Fe-C-Mn-V steels were produced by Tata Steel as 3 mm thick hot-rolled plates. The chemical composition of the alloys is listed in Table 1. The two steels have different carbon and vanadium contents, therefore, they are referred to as LCLV (low carbon - low vanadium alloy) and HCHV (high carbon - high vanadium alloy) in this study, whereas the content of other alloying elements is kept as low as possible. The HCHV steel contains twice the fraction of vanadium and carbon with respect to the LCLV steel and the atomic ratio of V:C is 1:1 in both steels.

Rectangular dilatometry specimens with dimensions $14 \times 10 \times 1\ mm^3$ are machined from the centre of the as-received plates. These specimens are heat treated in a DIL-805 A/D dilatometer in which inductive heating under a low pressure of 10^{-4} mbar is used, while cooling is achieved by a flow of helium gas. An S-type thermocouple is spot-welded in the centre of the specimen surface in order to control and monitor the temperature during the thermal cycle. The change in length of the specimen is recorded as a function of temperature and the obtained dilatometry data are used to study the phase transformation kinetics in each treatment. Micro-segregation of alloying elements like manganese and vanadium is considered not significant based on Electron Probe Micro-Analysis (EPMA), therefore no prior homogenisation treatment of the steels is performed.

The heat treatments performed in the dilatometer are schematically shown in Fig. 1. The specimens are heated to a high temperature (1050 °C for the LCLV and 1100 °C for the HCHV steel) in the austenitic region for 15 min. These temperatures are chosen to be 50 °C above the precipitates' dissolution temperature in each steel as predicted by the Thermo-Calc software [41]. The precipitates' dissolution temperatures are 994 °C and 1050 °C for the LCLV and HCHV steels, respectively (see Fig. 2). One specimen of each alloy is quenched to room temperature after soaking. These specimens are used to measure the prior austenite grain size (PAGS) with a KEYENCE VHX-5000 Digital Optical Microscope, which is calculated according to the equivalent diameter criterion in ImageJ software

Table 1
Chemical composition of the steel samples in weight percent (wt%) and atomic percent (at%) with balance Fe.

Steel		C	Mn	V	Si	P	Mo	Cu	Nb	S	Cr	Al	N	Ti
LCLV	wt%	.07	1.84	.29	.010	.0010	<0.005	<0.005	<0.0010	.0016	.010	.004	<0.001	.0001
	at%	.33	1.86	.32	.026	.0018	<0.003	<0.004	<0.0006	.0028	.011	.008	<0.004	.0001
HCHV	wt%	.14	1.83	.57	.013	.0010	<0.005	<0.005	<0.0010	.0010	.007	.008	<0.001	.0007
	at%	.62	1.85	.62	.026	.0018	<0.003	<0.004	<0.0006	.0017	.007	.002	<0.004	.0008

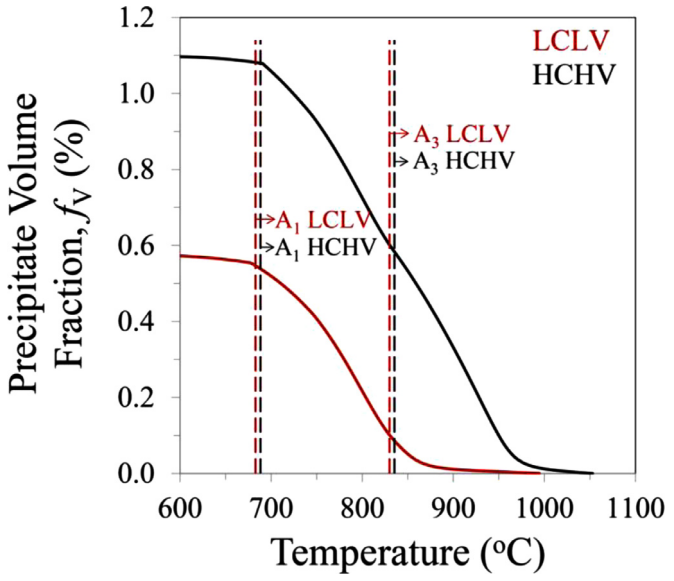

Fig. 2. Precipitate volume fraction versus temperature and the A_1 and A_3 transition temperatures for the LCLV and HCHV steels as predicted by ThermoCalc [41].

[42]. The specimens have been prepared by following the standard metallographic preparation procedure, which includes grinding, polishing to 1 µm and etching with picric acid. The other specimens are cooled at a rate of 15 °C/s from the soaking temperature to a lower temperature (900, 750 or 650 °C), where an isothermal annealing is applied for different holding times (10 s, 30 s, 1 min, 2 min, 5 min, 7 min, 10 min, 20 min, 45 min, 2 h and 10 h). The isothermal holding temperatures have been chosen based on the ThermoCalc [41] predictions presented in Fig. 2, aiming to study the precipitation kinetics in austenite, during the austenite-to-ferrite phase transformation and in ferrite. Analysis of the dilatometry data indicates that the phase transformation takes place only during the isothermal holdings and not during cooling from the soaking temperature to the isothermal holding temperature. The thermal cycle is completed by a rapid quench to room temperature.

The microstructural evolution of the LCLV and HCHV steels during annealing at the three isothermal holding temperatures is revealed by means of Scanning-Electron Microscopy (SEM). The SEM measurements are performed at room temperature using a JEOL JSM 6500F microscope on the specimens previously treated in the dilatometer. The specimens are prepared for SEM following the metallographic preparation procedure described above and finally etched with 2% Nital.

Rectangular specimens with dimensions $10 \times 10 \times 1\,mm^3$ are machined from the dilatometry treated specimens and measured at room temperature by Small-Angle Neutron Scattering. The aim is to study the precipitation kinetics of the LCLV and HCHV steels at the three isothermal temperatures mentioned above. The SANS measurements are performed on the Larmor Instrument at the ISIS Neutron and Muon Source (STFC Rutherford Appleton Laboratory). A 5×5 mm^2 neutron beam and a wavelength range of 0.42–1.33 nm are used. Wavelengths smaller than 0.42 nm are not considered to avoid effects from multiple Bragg scattering. A 3473–70 GMW electromagnet is used to generate a transversal magnetic field of 1.65 T, perpendicular to the neutron beam. This strong magnetic field is necessary to magnetically saturate the specimens, avoid any contribution to the scattering signal from magnetic domains, and separate the nuclear and magnetic scattering contribution from the SANS pattern. The SANS detector is a 600×600 mm^2 ^{3}He tube array with an 8×8 mm^2 pixel size at a distance of 4.3 m from the sample. Each specimen is exposed to the neutron beam for 35 min. The SANS data analysis is performed using the Mantid software [43].

The type of precipitation (interphase/random) as well as the precipitate shape and size are identified by TEM. The TEM analysis is performed on the LCLV and HCHV samples that are isothermally annealed at the temperature of 650 °C. A JEOL JEM-2200FS Transmission Electron Microscope with an accelerating voltage of 200 kV and a resolution of 1.3 Å is used. Thin foils are prepared by grinding the specimens to 100 µm and disks of a diameter of 3 mm are punched out from these thin foils. The extracted disks are electropolished in a twin-jet Struers Tenupol-3, electro-polishing setup at 19 V and a pump flow rate of 12 l/min at 20 °C. The electrolyte solution consisted of 5% perchloric acid ($HClO_4$) and 95% acetic acid (CH_3COOH). The imaging is carried out in the scanning mode (STEM) of the instrument during the measurements.

Atom Probe Tomography is used for the dilatometry heat-treated samples of LCLV and HCHV steels annealed at 650 °C to study the evolution of chemical composition, shape and morphology of precipitates during annealing. The specimens annealed for 5 min, 45 min and 10 h at 650 °C for both compositions are analysed by APT to capture the precipitates' growth and coarsening kinetics. More than 5 tips are extracted from each specimen to optimize the statistics of the APT cluster analysis.

The specimens are prepared by the lift-out method using Focussed Ion Beam milling (FIB) [44]. A last sputtering with 5 kV and 44 pA is applied to reduce the effect that the Gallium beam causes on the tips. After the FIB procedure, the tips are coated using an electron-beam induced Cobalt deposition [45] in order to limit Carbon diffusion along the shank [46]. The APT specimens are measured in a LEAP 4000X-HR system from CAMECA Instruments. Laser-assisted excitation is used with a pulse energy of 35 - 50 pJ, a pulse rate of 65–125 kHz, and a specimen base temperature of ~20 K.

The IVAS 3.8.0 software package from CAMECA Instruments is used for the APT data reconstruction and analysis. The entire analysis is based on isotope distribution (Mass-to-Charge-State Ratio - Da) [47]. The vanadium peaks are detected in 17, 25 and 25.5 Da in the Mass-to-Charge-State Ratio Spectrum, while carbon peaks are detected at 6, 6.5, 12 and 13 Da. Frequency distribution analysis for the elements proves that vanadium and carbon are clustered.

3. Results and discussion

3.1. Phase transformation kinetics

3.1.1. Phase transformation kinetics at 900 and 750 °C

The PAGS is measured in the specimens directly quenched from the austenitization temperature to room temperature and the average values are 63±3 µm for the LCLV and 62±2 µm for

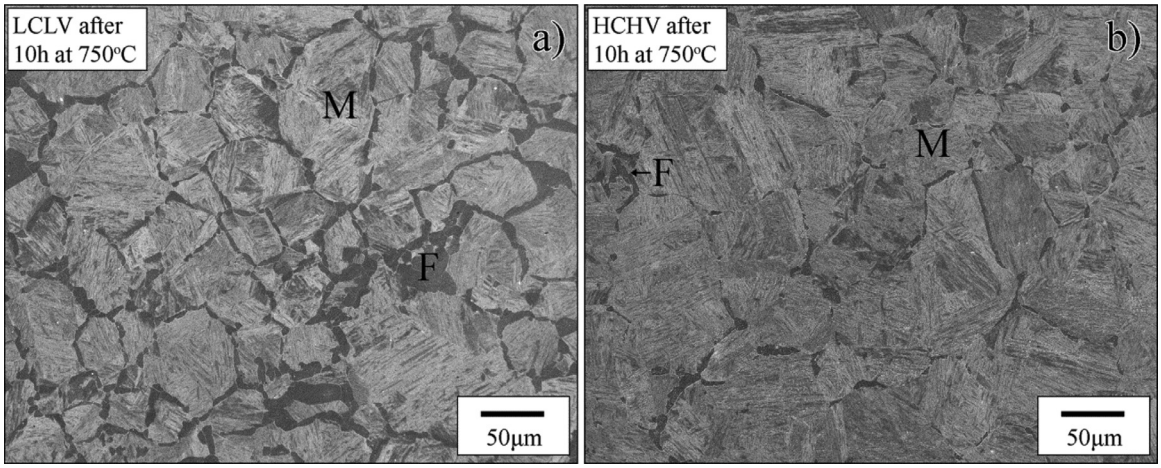

Fig. 3. SEM micrographs of the a) LCLV and b) HCHV samples isothermally annealed at 750 °C for 10 h. The existent ferritic (F) and martensitic (M) areas are indicated.

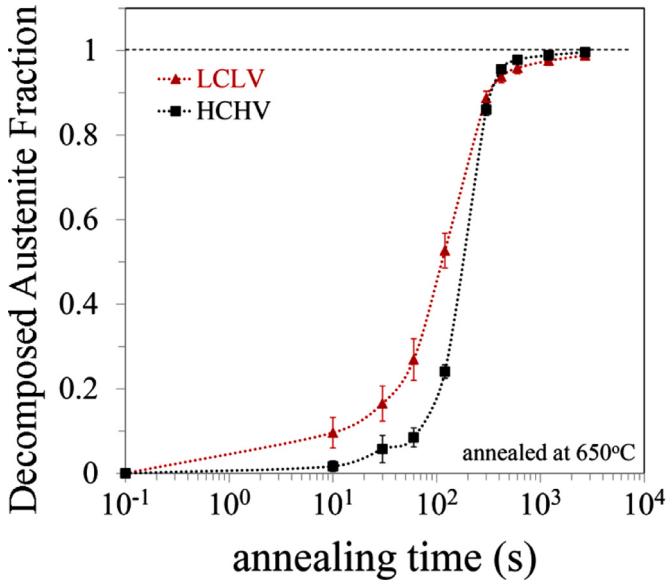

Fig. 4. Austenite to ferrite and pearlite phase transformation kinetics of LCLV(▲) and HCHV(■) steels during isothermal annealing at 650 °C (from dilatometry). According to SEM, the fraction of pearlite formed can be neglected.

the HCHV steel. Consequently, differences in the microstructural evolution of the two steels during annealing cannot be attributed to PAGS effects.

Analysis of the dilatometry data reveals no phase transformation in the LCLV and HCHV steels during annealing at 900 °C. This temperature is above the theoretical A_3 equilibrium temperatures, predicted by ThermoCalc [41] to be 830 °C and 834 °C in the LCLV and HCHV steels, respectively (Fig. 2). At 750 °C, only a very small fraction of ferrite is formed in the LCLV steel after 10 h of annealing, while almost no transformation is taking place in the HCHV steel. Fig. 3a and b shows the SEM micrographs of the LCLV and HCHV specimens annealed at 750 °C for 10 h, respectively. As seen in Fig. 3a, a small fraction of allotriomorphic ferrite is formed in the LCLV steel after 10 h, while the microstructure is almost fully martensitic for the same conditions in HCHV steel in Fig. 3b, confirming the dilatometry data interpretation.

3.1.2. Phase transformation kinetics at 650 °C

At 650 °C, austenite transforms into ferrite in both steels according to the dilatometry curves. Fig. 4 shows the fraction of transformed phase during annealing at 650 °C for LCLV and HCHV steels as a function of annealing time. In both steels, more than 97% of the initial austenite is transformed after 20 min isothermal holding at 650 °C, so the final microstructure of the samples annealed for longer times mainly consists of ferrite. For shorter times, the microstructure consists of a mixture of ferrite and martensite. The martensite forms from the untransformed austenite during the final quenching to room temperature. According to Fig. 4, the onset of the austenite-to-ferrite phase transformation is delayed in the HCHV steel compared to the LCLV steel. This can be attributed to the higher carbon content of the HCHV steel, which stabilizes the austenite and delays the onset of phase transformation. In addition, vanadium can retard ferrite nucleation due to segregation of micro-alloying elements at the grain boundaries of austenite [48]. Based on theoretical TTT (time-temperature-transformation) diagram calculations using the program MUCG83 [49], the effect of carbon on the delay of the onset of phase transformation is stronger than the effect of vanadium in these steels.

Representative SEM images showing the microstructural evolution during annealing at 650 °C for both steels are presented in Fig. 5. Fig. 5a, c and e is related to the LCLV steel specimens annealed for 2 min, 10 min and 10 h, respectively, while the micrographs in Fig. 5b, d and f correspond to HCHV specimens annealed for 1 min, 7 min and 10 h, respectively. The existent ferritic (F), martensitic (M) and pearlitic (P) areas are indicated in each condition. The SEM analysis shows the local formation of a small fraction of pearlite in both steels. The cementite precipitation is observed after 2 min of annealing in the LCLV steel and after 1 min in the HCHV steel, as shown in Fig. 5a and b.

3.2. Precipitation kinetics

3.2.1. Analysis method of the small-angle neutron scattering data

The Small-Angle Neutron Scattering intensity is a 2D pattern that reflects the macroscopic differential scattering cross-section, $(d\Sigma/d\Omega)(\boldsymbol{Q})$. This is a function of the scattering vector, $\boldsymbol{Q}$, and is obtained from the SANS intensity after background correction and calibration of the neutron flux considering the detector efficiency and sample transmission [50]. The $(d\Sigma/d\Omega)(\boldsymbol{Q})$ may have two components because of the two different interactions of neutrons with matter. Neutrons interact with the nuclei of the atoms via nuclear forces, leading to the nuclear cross-section, $(d\Sigma/d\Omega)_{NUC}(Q)$, and with the magnetic moments of the unpaired electrons through the dipole-dipole interaction [35], leading to the magnetic cross-section, $(d\Sigma/d\Omega)_{MAG}(Q)$. The selection rules for the magnetic scattering are such that neutrons "see" only the

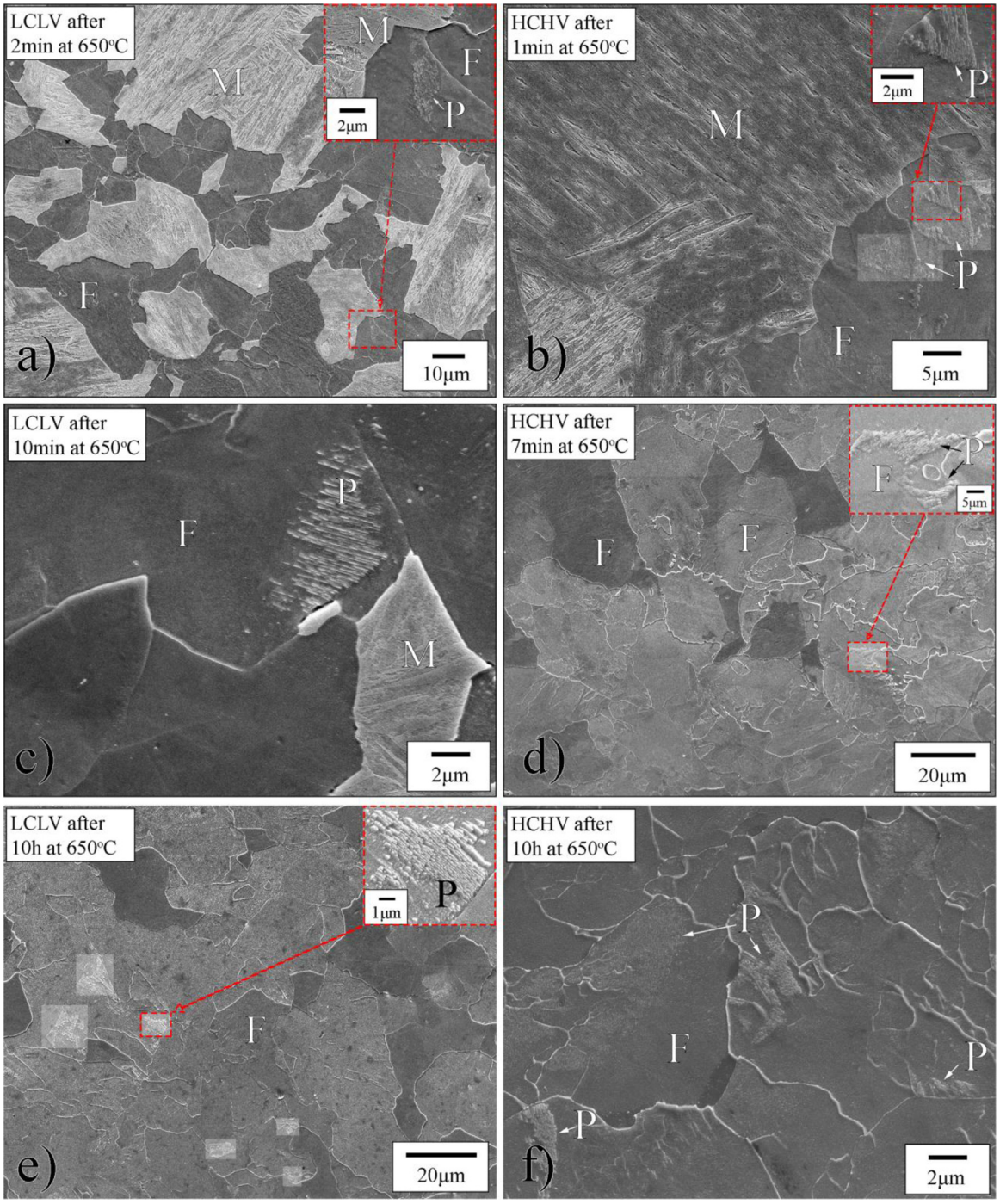

Fig. 5. SEM micrographs of the LCLV and HCHV steels isothermally annealed at 650 °C for different times and subsequently quenched to room temperature. Microstructure of LCLV specimens annealed for a) 2 min, c) 10 min and e) 10 h and of HCHV specimens annealed for b) 1 min, d) 7 min and f) 10 h. The existent ferritic (F), martensitic (M) and pearlitic (P) areas in each condition are indicated.

magnetization components that are perpendicular to the scattering vector, ***Q***. Thus, if an external magnetic field is high enough to saturate the magnetization and is applied along a direction contained in the detector plane, the macroscopic differential scattering cross-section can be written as [35]:

$$\left(\frac{d\Sigma}{d\Omega}\right)(Q) = \left(\frac{d\Sigma}{d\Omega}\right)_{NUC}(Q) + \left(\frac{d\Sigma}{d\Omega}\right)_{MAG}(Q)\cdot \sin^2\alpha, \qquad (1)$$

where α is the angle between the magnetic field direction and ***Q***. In this way it is possible to distinguish between the nuclear and magnetic contribution to the scattering. For this purpose, we consider sectors of 30°, parallel and perpendicular to the magnetic field, leading to $(d\Sigma/d\Omega)_{NUC}$ and $(d\Sigma/d\Omega)_{NUC}+(d\Sigma/d\Omega)_{MAG}$, respectively, and to $(d\Sigma/d\Omega)_{MAG}$ as the difference between these results. We then obtain quantitative information on the precipitation kinetics in the steel matrix by a detailed analysis of the nuclear differential scattering cross-section, which for a dilute system of precipitates within a homogeneous matrix is given by [50]:

$$\left(\frac{d\Sigma}{d\Omega}\right)_{NUC}(Q) = (\Delta\rho_{NUC})^2 \int D_N(R)\cdot V^2(R)\cdot P^2(Q,R)dR, \qquad (2)$$

with R and V the precipitate radius and volume (for spherical precipitates it is $V=4/3\pi R^3$) respectively. The log-normal number distribution, $D_N(R)$, is assumed to be given by:

$$D_N(R) = \frac{N_p}{R\sigma\sqrt{2\pi}} \exp\left\{-\frac{[\ln(R) - \ln(R_m)]^2}{2\sigma^2}\right\} \quad (3)$$

where N_p is the precipitate number density, R_m is the mean precipitate radius and σ is the standard deviation of the size distribution. The precipitate volume distribution is the product $D_V(R)=D_N(R)\cdot V$.

$P(Q,R)$ is the form factor describing the precipitate shape, which for spherical precipitates is $P(Q,R)=3[sin(QR)-(QR)cos(QR)]/(QR)^3$ [50,51].

Finally, $\Delta\rho_{NUC}$ is the difference in nuclear scattering length density between the matrix and the precipitates (nuclear contrast) and is given by $\Delta\rho_{NUC}=\rho_{Fe}$ - $\rho_{VC} \approx {N_o}^{Fe}\ {b_c}^{Fe}$ - ${N_o}^{VC}\ {b_c}^{VC}$. The term N_o is the number density calculated for Fe and VC considering their bulk density, ρ_m, and their molecular weight, M, using $N_o=N_A\ \rho_m/M$, yielding the number density of Fe atoms ${N_o}^{Fe}=84.9\ nm^{-3}$ and of VC, with the stoichiometric ratio of $V/C=1$, ${N_o}^{VC}=55.1\ nm^{-3}$. N_A is Avogadro's number and b_c is the coherent scattering length. The scattering length of the matrix and the precipitates is ${b_c}^{Fe}=9.45\times10^{-15}$ m and ${b_c}^{VC}=6.26\times10^{-15}$ m, respectively, resulting in $\rho_{Fe}=\ 8.02\times10^{-4}\ nm^{-2}$ for iron and $\rho_{VC}=3.46\times10^{-4}\ nm^{-2}$ for the vanadium carbides, and eventually in ${\Delta\rho_{NUC}}^2=20.8\times10^{-8}\ nm^{-4}$.

The precipitate volume fraction, f_V, is calculated by integrating the area under the $[Q,Q^2(d\Sigma/d\Omega)_{NUC}]$ curve, which is commonly known as Kratky Plot. For a dual-phase system, the area $Q_{o,NUC}$ below the Kratky Plot is [35]:

$$Q_{o,NUC} = \int_0^\infty \left(\frac{d\Sigma}{d\Omega}\right)_{NUC} Q^2 dQ = 2\pi^2(\Delta\rho_{NUC})^2 f_V(1-f_V) \quad (4)$$

When the precipitate volume fraction is low, the above equation is simplified to:

$$f_V \cong \frac{Q_{o,NUC}}{2\pi^2(\Delta\rho_{NUC})^2} \quad (5)$$

The precipitation kinetics of both steels during annealing at 900, 750 and 650 °C is discussed below based on the resulting SANS measurements.

3.2.2. Precipitation kinetics at 900 and 750 °C

The SANS intensity of the LCLV and HCHV steels that have undergone an isothermal annealing treatment at 900 and 750 °C for 10 h is compared to the corresponding intensity of the specimen of each steel that is directly quenched from the soaking temperature to room temperature and does not contain any precipitates. No significant differences are observed, leading to the conclusion that precipitates are not detected in any in these conditions. The SANS intensity curves of the samples annealed at 900 and 750 °C are not presented in the main text but can be found in the supplementary material of this manuscript.

The absence of precipitates at 900 and 750 °C in both steels is closely related to the (near) non-occurrence of the austenite to ferrite phase transformation as discussed during the interpretation of the dilatometry and SEM data in section A.1. Since the austenite-to-ferrite phase transformation does not take place at 900 °C in any of the steels nor at 750 °C in the HCHV steel, and due to the high solubility of the vanadium carbide precipitates in austenite, precipitates are not formed in these conditions, which is in agreement with ref. [15]. Precipitates are also not detected in the LCLV steel at 750 °C after 10 h of isothermal holding despite the transformation of a small fraction of austenite into ferrite in this steel. Nucleation of precipitates might have started in this condition, however, the precipitates size and volume fraction are expected to be extremely small, i.e. below 1 nm and 0.1%, respectively, and, therefore, not detectable by the SANS technique.

Moreover, it is worth mentioning here that ThermoCalc [41] equilibrium calculations are not in agreement with our studies, since ThermoCalc predicts precipitation and phase transformation at 750 °C in both steels and precipitation at 900 °C for the HCHV alloy (Fig. 2). The difference between our experimental results and ThermoCalc could be attributed either to the Gibbs-Thomson effect, which could be significant for small nano-sized precipitates, or to the fact that the system has not reached equilibrium after 10 h of annealing.

The equilibrium concentration of vanadium in the matrix taking into account the Gibbs-Thomson effect is given by [52]

$$X_{eq,r} = X_{eq,\infty} \exp\left(\frac{2\gamma\upsilon_{at}^{VC}}{X_p r k T}\right) \quad (6)$$

In the equation above, $X_{eq,\infty}$ is the solubility limit of vanadium in ferrite according to ThermoCalc, γ the interface energy between the precipitates and the ferritic matrix, ${\upsilon_{at}}^{VC}$ the average atomic volume of the vanadium carbides, X_p the equilibrium mole fraction of vanadium in the VC-precipitates calculated by ThermoCalc, r the precipitate radius, k_B the Boltzmann constant and T the temperature. For precipitates with an average radius in the range 1.1–2 nm and for typical precipitate-ferritic matrix interface energy values in the range 0.2–0.8 J/m^2 [53], the resulted $X_{eq,r}$ at 750 and at 900 °C is very close to the $X_{eq,\infty}$ and always smaller than the total amount of vanadium in both steels. This means that the increase in the solubility limit of vanadium in the matrix due to the increase in Gibbs free energy of the precipitates (attributed to the Gibbs Thomson effect) is very small and not sufficient to prevent precipitation in the steels. Based on the above calculations, we conclude that the Gibbs Thomson effect cannot – on its own - explain the difference between the experimental results and equilibrium ThermoCalc calculations, and other kinetics factors may also play a role.

The most possible explanation is that the system is far from equilibrium after 10 h at 750 and 900 °C for both alloys. According to ThermoCalc, the maximum ferrite fraction that can form at 750 °C is 86% and 87% for the LCLV and the HCHV, respectively. As a result, a maximum precipitate volume fraction that could form would be 0.42 and 0.95% in the LCLV and the HCHV steels, respectively. At 900 °C, ferrite formation is not predicted by ThermoCalc in either of the steels, however, precipitation of a maximum of 0.3% would be possible in the HCHV steel. The equilibrium conditions predicted by ThermoCalc could be reached by applying longer annealing times at 750 and 900 °C.

3.2.3. Precipitation kinetics at 650 °C

The SANS nuclear differential scattering cross sections of the LCLV and HCHV steels annealed at 650 °C are shown in Fig. 6a and b, respectively. The corresponding magnetic components are presented in Fig. 6c and d. For the sake of simplicity we only show the scattering curves obtained at the most informative annealing times (30 s, 2 min, 5 min, 20 min, 45 min, 2 h and for 10 h at 650 °C). The nuclear and magnetic scattering cross sections of the direct-quenched specimens are also provided.

SANS is used to study the precipitation kinetics in the LCLV and HCHV steels, in which it should be kept in mind that the dislocations from the martensite phase also contribute to the SANS pattern. The analysis of the precipitation kinetics that is explained below refers to both LCLV and HCHV steels as their nuclear scattering cross sections follow the same trend during annealing.

For the specimens of both steels annealed for less than 2 min at 650 °C, the SANS intensity follows a Q^{-4} power law (Porod's Law), indicating that scattering originates from large-scale objects like grain boundaries and interfaces [37,50,54]. In the absence of

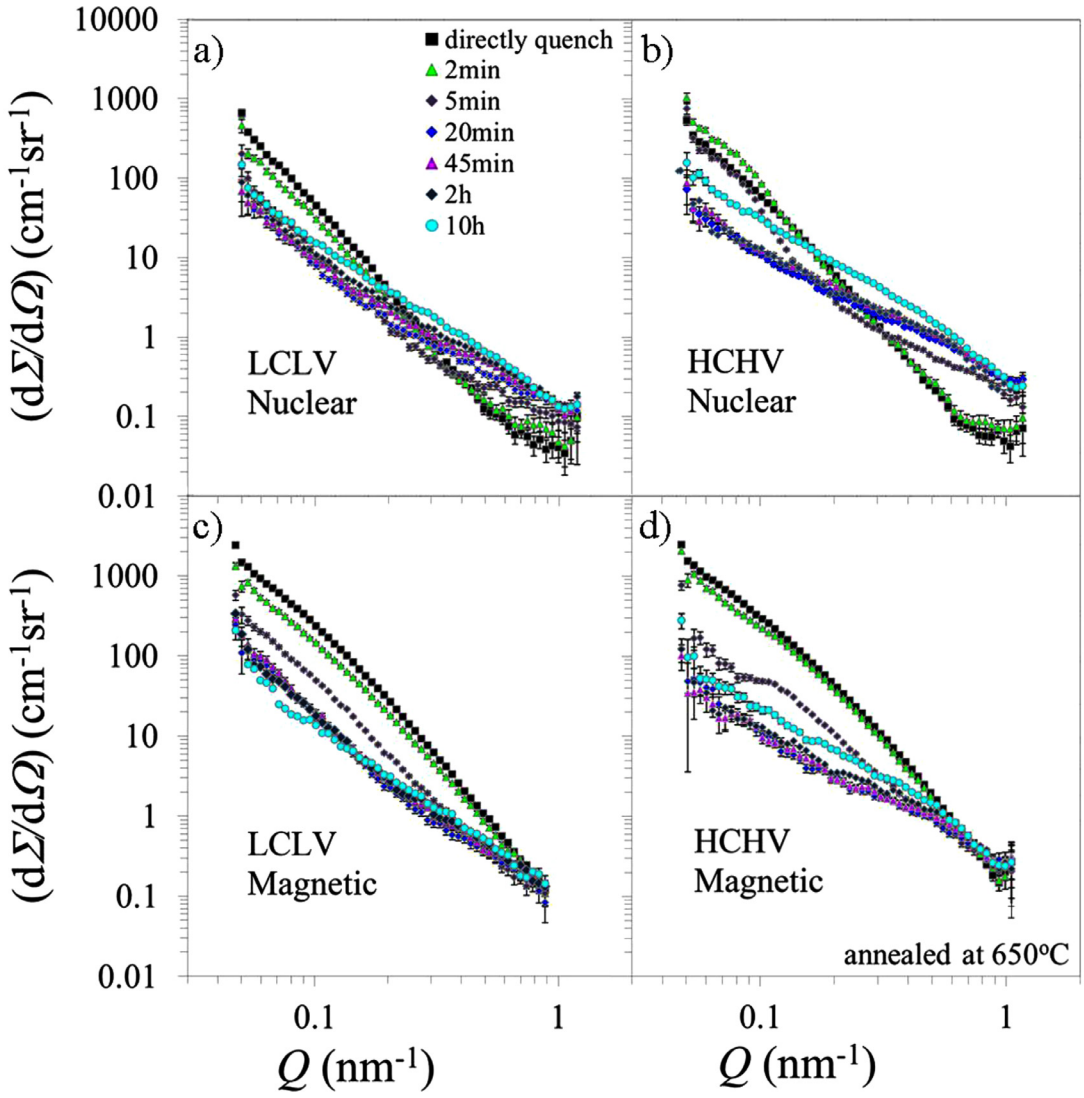

Fig. 6. Nuclear differential scattering cross section of a) LCLV and b) HCHV steel as a function of Q measured at room temperature after annealing at 650 °C for up to 10 h. The corresponding magnetic differential scattering cross sections are plotted in c) and d) for LCLV and HCHV steel, respectively. The scattering curves of the samples heat-treated at the most representative conditions are shown.

deviations from the Q^{-4} power law, we conclude that neither precipitation nor phase transformation have started.

Between 2 and 20 min of annealing, a decrease in the nuclear intensity is observed in the low-Q area ($Q < 0.2$ nm^{-1}). The $(d\Sigma/d\Omega)_{NUC}$ at low-Q values originates from large objects like grain boundaries, dislocations and large precipitates [37,50,54]. Therefore, the decrease in the $(d\Sigma/d\Omega)_{NUC}$ in the low-Q area of the 2 - 20 min curves is attributed to the phase transformation through the decrease of the fraction of martensite (which forms directly after the quench from 650 °C to room temperature and contains high dislocation and grain boundary densities) in agreement to the phase transformation kinetics curve in Fig. 2. For higher Q values, in the 2–20 min curves, an increase in $(d\Sigma/d\Omega)_{NUC}$ is observed, originating from the scattering of small precipitates. For annealing times longer than 20 min, when the phase transformation is almost complete, additional scattering is observed over the whole Q range. In the low-Q range, the major contribution to the signal comes from cementite as well as from the large VC precipitates. The small increase in $(d\Sigma/d\Omega)_{NUC}$ in the high-Q area is caused by smaller precipitates.

The magnetic scattering cross sections of the LCLV and HCHV steels, depicted in Fig. 6c and d, do not show the same Q dependence and time evolution as the corresponding nuclear scattering cross sections, indicating different nuclear and magnetic structures in our steels. A decrease in $(d\Sigma/d\Omega)_{MAG}$ curves is observed over the entire Q range in both steels up to 2 h of annealing while an increase is observed for longer annealing times. The martensitic phase having a high dislocation density, large number of Low-Angle Grain Boundaries (LAGB) and iron carbides may pin the walls between the magnetic domains and hinder their alignment along the magnetic field. The precipitation of cementite and the formation of pearlite also affect the magnetic SANS intensity, but this feature is not further analysed in this paper.

Quantitative information on the precipitation kinetics is obtained from Kratky plots, $Q^2(d\Sigma/d\Omega)_{NUC}$ plotted as a function of Q. Fig. 7a and b shows such plots for different annealing times at 650 °C of LCLV and HCHV for some representative conditions. For an accurate analysis of the VC precipitation kinetics by SANS, only the scattering from the precipitates is considered whereas all other contributions are subtracted.

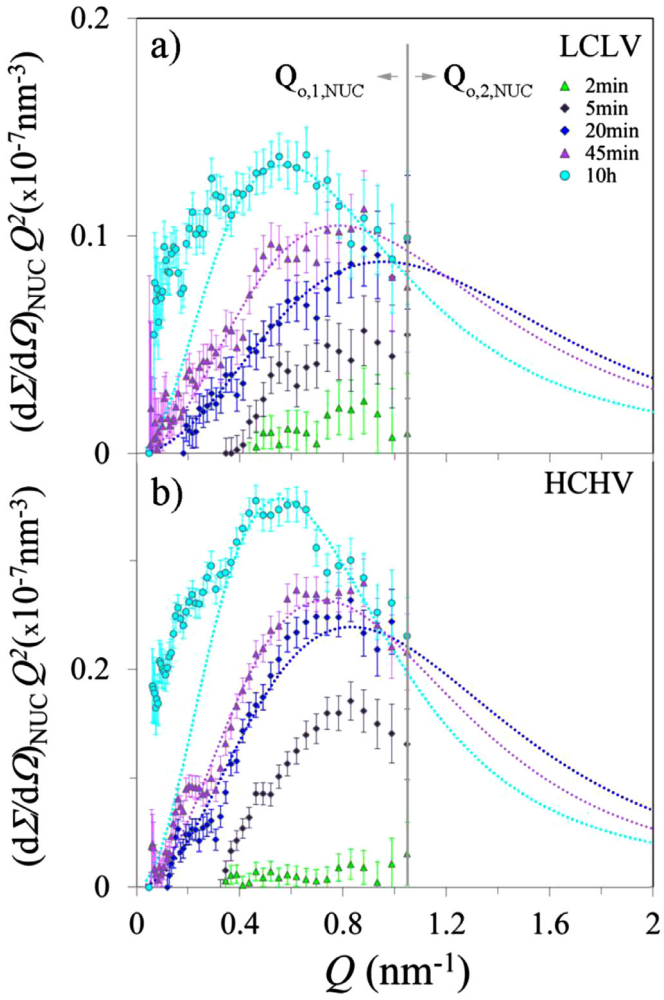

Fig. 7. Time evolution of $Q^2(d\Sigma/d\Omega)_{NUC}$ vs Q for the a) LCLV and the b) HCHV steel during holding at 650 °C for up to 10 h (data points), after background subtraction. The thinner dotted lines represent the theoretical $Q^2(d\Sigma/d\Omega)_{NUC}$ curves originating from the fitting.

During isothermal annealing, a progressive increase in the $Q^2(d\Sigma/d\Omega)_{NUC}$ intensity in both LCLV and HCHV steels is observed. As the holding time increases, the peak position of the curves gradually moves towards the lower Q area, reflecting the increasing precipitate size (growth or coarsening).

The experimentally derived Kratky plots are fitted to the theoretical Kratky-plot equation (Eq. (2) multiplied by Q^2) leading to the fitting parameters R_m, N_p and σ for each curve. The fitting is performed for the specimens of LCLV and HCHV steels annealed for times longer than 5 min at 650 °C. For shorter annealing times, the experimental $Q^2(d\Sigma/d\Omega)_{NUC}$ curves cannot be fitted as they have a completely flat profile (precipitates are not detected before 2 min as explained before).

The evolution of the precipitate mean radius, R_m, and number density, N_p, during annealing from 5 min to 10 h is shown in Fig. 8a and b, respectively. The precipitates' growth during annealing in both steels is reflected in the increase of the precipitate mean radius (Fig. 8a). A maximum precipitate radius of 1.5 and 1.8 nm is reached after 10 h of annealing for LCLV and HCHV steels, respectively.

Like the mean precipitate radius, the precipitate number density follows the same trend for both steels. The gradual increase in the precipitate number density (Fig. 8b) from the beginning of annealing and for the first 10 min at 650 °C suggests intense pre-

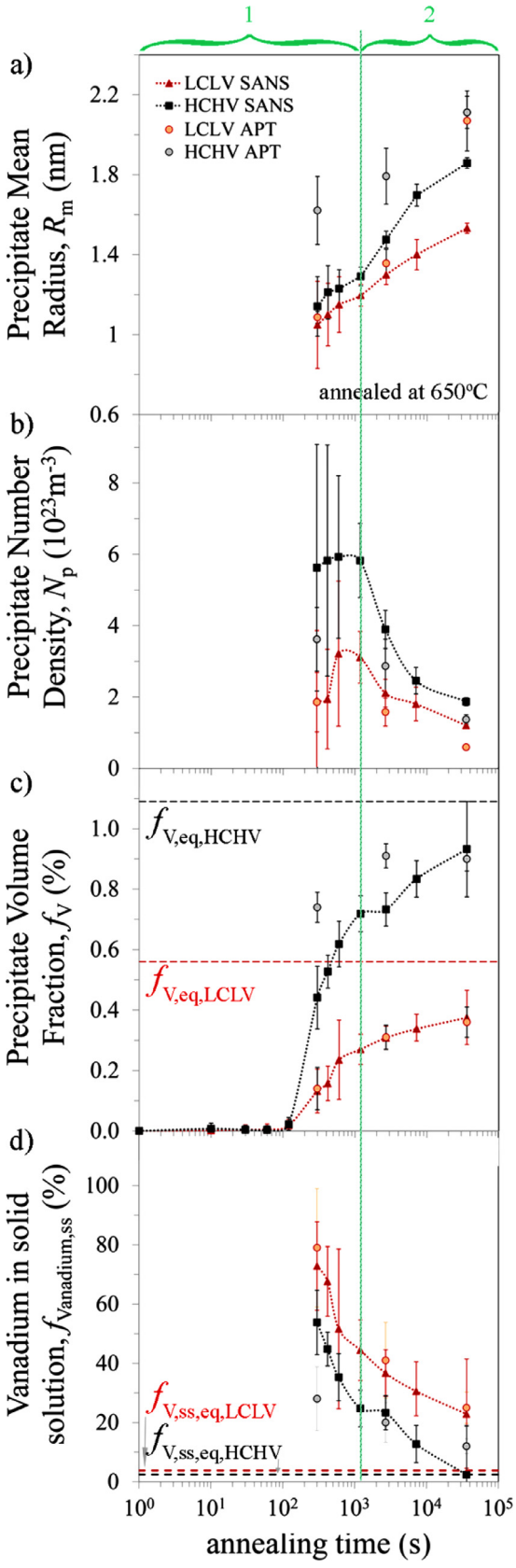

Fig. 8. Precipitate a) mean radius, R_m, b) number density, N_p, c) volume fraction, f_V, and, d) amount of vanadium in solid solution, $f_{vanadium,ss}$, evolution during annealing at 650 °C for the LCLV(▲) and HCHV(■) steels. During time period 1, phase transformation takes place and precipitate nucleation and growth are dominant. In period 2, phase transformation is almost complete (>97% of austenite transformed) and precipitate growth (with overlapping diffusion fields) and coarsening take place. The dashed lines indicate the equilibrium values calculated by ThermoCalc [41].

cipitate nucleation. Between 10 and 20 min of annealing, the precipitate number density remains constant while their radius is increasing, indicating that precipitate growth is the dominant phenomenon. We define as time period 1 the first 20 min of annealing and period 2 from 20 min to the end of annealing. During period 2, the precipitate number density continuously decreases due to precipitate coarsening.

At the beginning of annealing the precipitates are small and their size is comparable to the resolution of the SANS instrument, leading to larger error bars in the precipitate mean radius (Fig. 8a) and number density (Fig. 8b). Additionally, the background contribution from dislocations decreases with time and fitting the Kratky-plot curves results in lower error values for longer annealing times.

As shown in the $(d\Sigma/d\Omega)_{NUC}$ (Q) curves of Fig. 6a and b, the Q range of the nuclear differential scattering cross sections is restricted to $0.04 \leq Q \leq 1.05$ nm^{-1}, limiting the Q range of the Kratky-plot curves (Fig. 7a and b) and, consequently, leading to an underestimation of the precipitate volume fraction, f_V, if only this Q-range is used for the integration. For an accurate volume fraction determination, first the area below the $Q^2(d\Sigma/d\Omega)_{NUC}$ curves, $Q_{o,NUC}$, is calculated as the sum of $Q_{o,1,NUC}+Q_{o,2,NUC}$, and then the precipitate volume fraction is derived from Eq. (5). $Q_{o,1,NUC}$ is the area below the curve determined by the data in the Q range 0.04 - 1.05 nm^{-1}. These data are calculated by multiplying $(d\Sigma/d\Omega)_{NUC}(Q)$ (corrected after background subtraction) with Q^2, as described above. $Q_{o,2,NUC}$ is the area below each dotted Kratky plot for Q values between 1.05 and 2 nm^{-1} (Fig. 7a and b). The dotted curve is the theoretical calculated Kratky plot curve in the Q range 1.05 - 2 nm^{-1}. It is calculated for each annealed specimen using the R_m, N_p and σ values obtained from the fitting of the experimental Kratky plot in the Q range 0.04 - 1.05 nm^{-1}. Deviations between experiments and theory in the low Q range are most probably related to difficulties in the background subtraction.

The time evolution of the precipitate volume fraction during annealing at 650 °C is illustrated in Fig. 8c for both LCLV and HCHV steels. Before 2 min, no precipitates are detected and the measured precipitate volume fraction curve is practically zero. After 2 min, the volume fraction increases continuously, reaching a maximum 0.37 ± 0.09% for the LCLV steel and 0.93 ± 0.16% for the HCHV steel after 10 h of annealing. Precipitation takes place during and after the phase transformation and precipitates are measured in both steels when a certain volume fraction of ferrite is formed after 5 min. This is illustrated in Fig. 9a and b, in which the precipitation and phase transformation kinetics are plotted for the LCLV and HCHV steels, respectively. The enhanced precipitation during phase transformation is a result of solubility drop of the vanadium when austenite transforms to ferrite, giving rise to a high driving force for precipitation. The precipitates formed during the transformation are aligned in rows (interphase precipitation, see TEM image, Fig. 11, and APT maps, Fig. 12a and d), while those nucleating after the completion of the phase transformation are randomly dispersed and have a smaller diameter. The small increase in the nuclear scattering intensity in the high-Q area after 20 min of annealing at 650 °C, as shown in Fig. 6a and b, originates from these small precipitates.

The continuous increase in volume fraction after 20 min (Fig. 8c), combined to the increase in precipitate size (Fig. 8a) and the decrease in precipitate number density (Fig. 8b), indicates combined precipitate growth and coarsening. Fig. 8d shows the evolution of the amount of vanadium in solid solution, $f_{vanadium,ss}$, in both alloys. It decreases rapidly during precipitate nucleation and growth (during time period 1) and continues decreasing till the end of the annealing treatment due to the combined growth and coarsening (period 2).

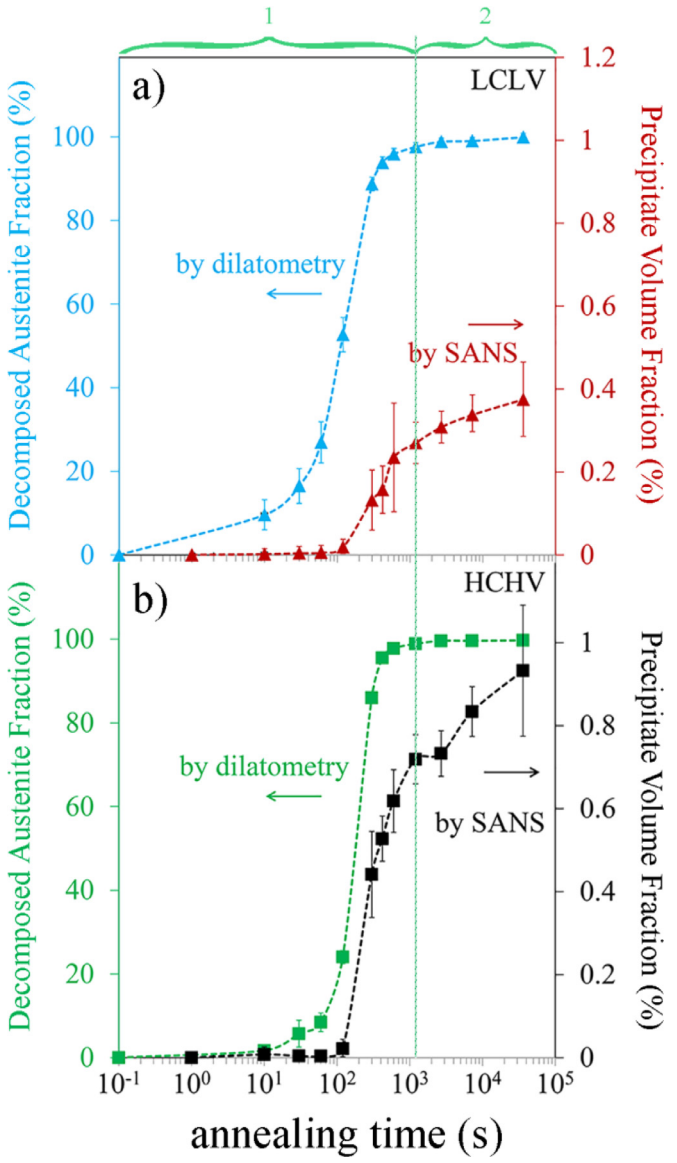

Fig. 9. Vanadium carbide precipitation and austenite-to-ferrite phase transformation kinetics (see Fig. 4) during isothermal annealing at 650 °C in the a) LCLV and b) HCHV steels. In both steels, precipitation takes place during and after the phase transformation. During time period 1, phase transformation takes place and precipitate nucleation and growth are dominant. In 2, phase transformation is almost complete (>97% of austenite transformed) and precipitate growth and coarsening take place.

The measured volume fraction, average precipitate size and number density of the precipitates are compared to the SANS results of previous studies of a steel with a similar that is annealed at 700 °C (instead of 650 °C) [20]. We observe similarities and important differences between annealing at 700 and 650 °C. We observe an increase in precipitate volume fraction in the LCLV steel from 0.13 to 0.37% from 5 min to 10 h of annealing at 650 °C, which is similar to the findings reported in Ref. [20], which reports an increase from 0.09 to 0.28% during annealing in the same time range at 700 °C in a steel with similar vanadium content. However, we measure small (<2 nm) spherical / slightly ellipsoidal precipitates with number density of $\sim 10^{23}$ m^{-3}, while in ref. [20], ~10 times larger disk-shape and oblate precipitates are detected with number density $\sim 10^{21}$ m^{-3}, suggesting that small changes, like a 50 °C change in the annealing temperature, lead to very different precipitation kinetics. The precipitate number density values deduced

from our SANS data are comparable to previous studies on vanadium carbides at the same temperatures for medium [18,24] and low-Carbon steels [19].

Thermodynamic calculations performed with the ThermoCalc software [41] give an equilibrium volume fraction for VC of 0.56% in the LCLV steel and 1.09% in the HCHV steel at 650 °C (Fig. 2), which is slightly higher than the values deduced by SANS. From these results, it is concluded that after 10 h of isothermal holding most of the vanadium is in the precipitates, but the volume fraction has not reached its maximum value.

The precipitation kinetics are found to have the same behavior in the LCLV and HCHV steels during annealing from 5 min to 10 h at 650 °C due to the same phase transformation kinetics in this time range. Due to the delay in the onset of austenite-to-ferrite phase transformation in HCHV steel compared to LCLV steel at 650 °C (Fig. 2), and considering the fact that precipitation of vanadium carbides is more favoured after the beginning of the phase transformation, a delay in precipitation kinetics in the HCHV steel is expected in order to follow the trend of the phase transformation curve. According to the phase transformation kinetics curves of Fig. 2, the delay should be observed during the first 5 min of annealing. However, because of the limitations of the SANS technique, precipitates are only detected after 5 min of annealing in both steels. Therefore possible differences in the start of the precipitation kinetics between both steels in the first 5 min of annealing cannot be observed.

Moreover, according to the dilatometry results in Fig. 2, after 5 min, the phase transformation kinetics for the LCLV and HCHV steels show similar behaviour. This is reflected in the precipitation kinetics which follows the same trend in both steels after 5 min as shown in Fig. 8a, b and c.

As a last step in the precipitation kinetics analysis, Fig. 10a and b shows the time evolution of the log-normal precipitate volume distribution of the VC precipitates in the LCLV and HCHV steels, respectively. The average precipitate size determines the peak position of the volume distribution curve while the area below each curve is the precipitate volume fraction at that time of annealing. For both steels, the peak area of the distribution increases with time until 20 min of annealing, without any shift in the peak position, indicating pronounced nucleation of small sized nuclei. After 20 min, the volume distribution curves broaden with increasing holding time, coupled with a decrease in peak height and a shift in the peak position to larger R values. We thus conclude that the growth and coarsening effect is dominant in this time range and is becoming stronger with holding time.

3.2.4. Precipitation characterization by tem and apt at 650 °C

Fig. 11 shows a representative bright-field TEM image of the HCHV specimen annealed at 650 °C for 20 min and subsequently quenched to room temperature. The precipitates are represented in black while the ferritic matrix is represented in grey. The precipitates are arranged in rows, showing that interphase precipitation takes place during the austenite-to-ferrite phase transformation during the first 20 min of annealing. The average distance between the rows (inter-sheet spacing) in this condition is approximately 12 nm. The precipitates' average radius is measured to be around 1.1 nm, in agreement with the value 1.3 ± 0.6 nm derived from the SANS measurements. In addition, spherical (or slightly ellipsoidal) precipitates are observed, which a posteriori justifies our SANS data analysis based on the modeling of spherical precipitates. The fact that the precipitates' shape is spherical is in agreement to previous studies [18,19,24], in which spherical/ellipsoidal [18,19] and spherical/disk-shaped [24] vanadium carbide precipitates were formed during isothermal annealing at the same temperature.

Representative 3D vanadium atom maps obtained by APT from samples of the LCLV and HCHV steels heat treated at 650 °C for

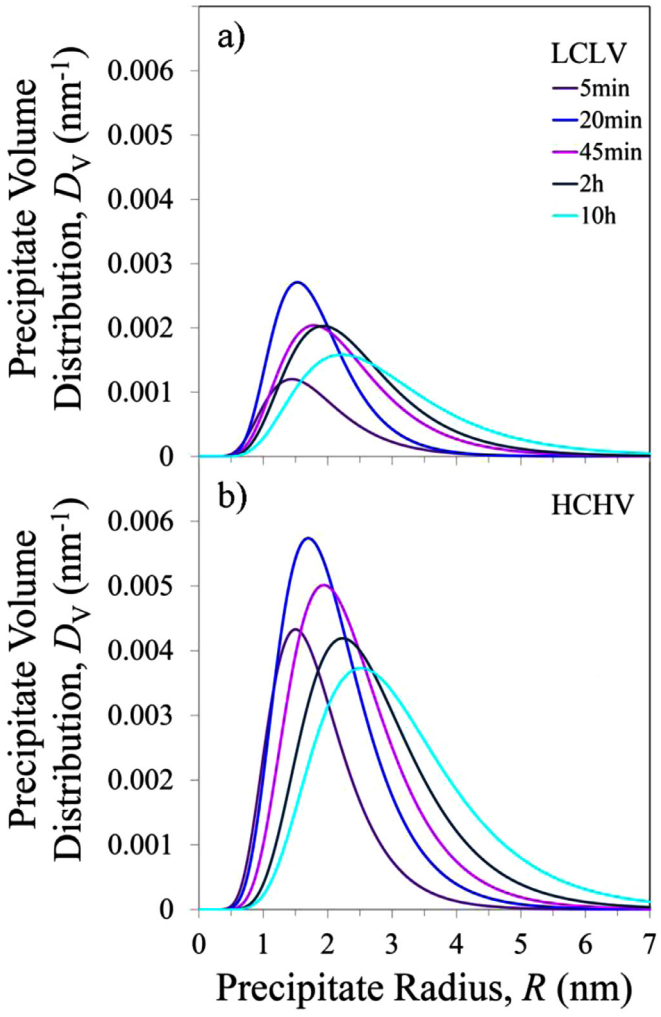

Fig. 10. Log-normal volume distribution, D_V, of the VC precipitates in the a) LCLV and b) HCHV steels during annealing at 650 °C for up to 10 h. The curves are based on the R_m, N_p and σ values resulted from the fitting of the experimental $Q^2(d\Sigma/d\Omega)_{NUC}$ results.

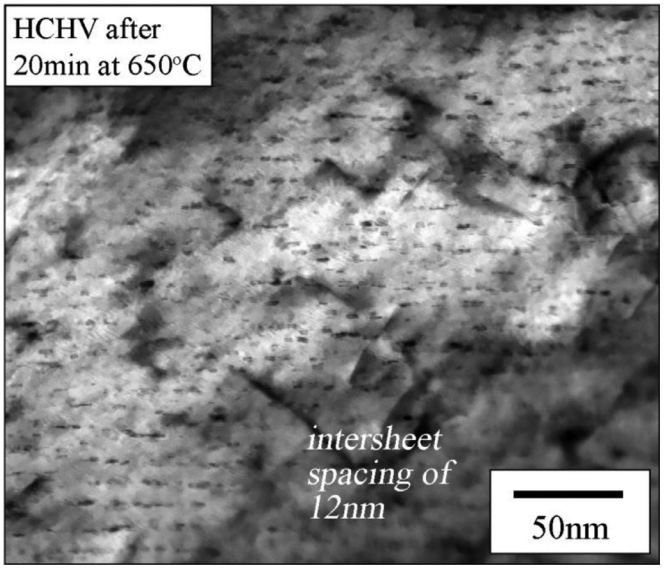

Fig. 11. Bright field TEM image illustrating interphase precipitation in the HCHV steel. It belongs to the specimen annealed for 20 min at 650 °C.

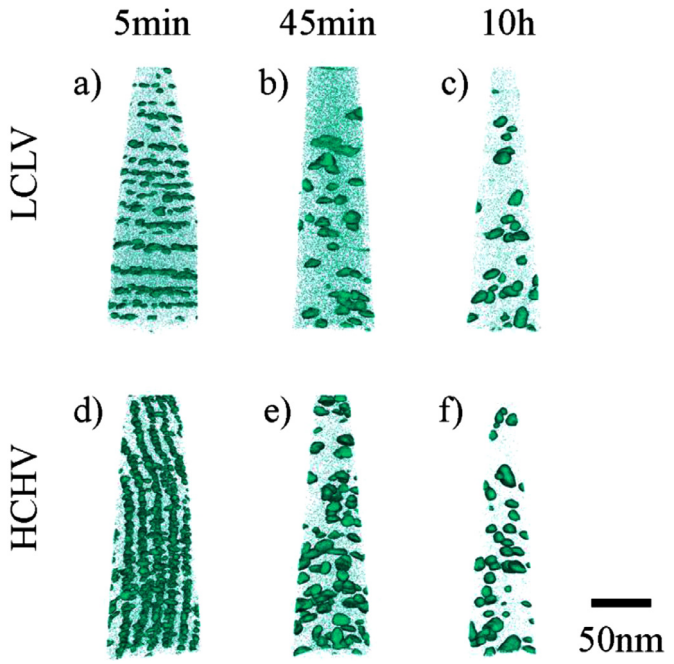

Fig. 12. 3D APT atom maps of V of a)-c) LCLV steel and d)-f) HCHV steel specimens previously treated in different conditions. The maps are superimposed with isoconcentration surfaces of 2at%V. The arrangement of the precipitates and their evolution during annealing is shown.

holding times of 5 min, 45 min, and 10 h are shown in Fig. 12a–c and d–f, respectively. The V-rich regions can be clearly seen in all maps, which are superimposed with 2 at.%V isoconcentration surfaces. This threshold of vanadium concentration is set to a value much larger than the steel nominal composition in order to avoid local vanadium concentration fluctuations. The 3D maps can be rotated in any orientation, providing information regarding the precipitates' shape and arrangement. In all these maps and for both steels, spherical and ellipsoidal precipitates are observed. Small precipitates with a high number density can be seen in Fig. 12a and d after 5 min of annealing at 650 °C of a LCLV and a HCHV specimen, respectively. Their size increases with annealing time as a result of growth and/or coarsening as shown in Fig. 12b, c, e and f, while their number continuously decreases. Moreover, precipitates aligned in parallel rows are observed in both steels (Fig. 12a and d), denoting interphase precipitation. Randomly distributed precipitates in the ferritic matrix are also present, as shown for instance in Fig. 12c.

From the vanadium maps, we deduced the inter-sheet spacing of interphase precipitation, determined by the velocity of the migrating α/γ interface during the austenite-to-ferrite phase transformation. The inter-sheet spacing is measured in the 5 min annealing condition in both steels, where coarsening has not started yet and the precipitates arrangement is relatively clear. It is found to be in the range of 12 - 17 nm in both steels, in agreement with our TEM measurements.

A quantitative characterization of vanadium carbide precipitates is obtained through a detailed cluster analysis. The cluster analysis is performed following the maximum separation method [55] based on solute vanadium atoms. Carbon enrichment is observed in the V-rich regions, indicating the presence of vanadium carbide precipitates. The maximum distance between two solute atoms that belong to the same cluster, d_{max}, and the minimum number of atoms in a cluster, N_{min}, are chosen as 1 nm and 20, respectively, after a trial and error procedure. The same d_{max} and N_{min} parameters are selected for all the measured specimens of LCLV and HCHV alloys. Clusters containing fewer atoms than N_{min} are not considered in the analysis to avoid the contribution of possible local fluctuations of vanadium concentration within the matrix. The d_{max} is determined based on the nearest neighbour distance (NN) distribution of 3 nearest neighbours.

The cluster analysis provides information regarding the precipitate size distribution, number density and volume fraction in the analysed tips. The precipitate number density is the number of precipitates divided by the analysed volume (volume of the tip), and the precipitate volume fraction is the total precipitate volume divided by the analysed volume. The precipitate volume is calculated from the number of vanadium atoms in each precipitate taking into account the unit cell volume of the VC and the number of vanadium atoms per unit cell. Four vanadium atoms are in one VC unit cell and its lattice parameter is 0.415 nm [31]. The radius of each precipitate is then calculated by assuming spherical precipitates. The detection efficiency of the instrument is 36% and it is considered in the above calculations to obtain the real number of the detected atoms.

Table 2 summarizes the precipitate radius, number density and volume fraction derived from APT measurements. The results obtained from the specimens of both steels, heat treated for the three annealing conditions, are compared to the corresponding values obtained from the SANS data analysis. The number of tips measured per condition by APT is given and R_m, N_p and f_V presented are the calculated average values of all the analysed tips per condition. Precipitates are detected in all the analysed tips of both alloys, except for 3 tips of the LCLV specimen annealed for 5 min. This is attributed to the low precipitate volume fraction (0.13%) in the LCLV steel after 5 min of annealing at 650 °C, and suggests non- homogeneous precipitate distribution over the entire specimen volume.

The precipitate mean radius, number density and volume fraction values obtained from the APT cluster analysis are in good agreement with the corresponding values derived from the SANS analysis as shown in Fig. 8a, b and c. The precipitate mean radius and volume fraction are continuously increasing in both steels during annealing at 650 °C, while the precipitate number density is decreasing from 45 min to 10 h due to precipitate coarsening.

The fraction of vanadium atoms in solid solution in ferrite during annealing can be also obtained from the APT cluster analysis. The fraction of vanadium in solid solution, $f_{vanadium,ss}$, is calculated for each tip as:

$$f_{vanadium,ss} = \left(N_{V,total} - N_{V,precip}\right)/N_{V,total} = N_{V,\alpha-Fe}/(N_{V,\alpha-Fe} + N_{V,precip}) \quad (7)$$

In Eq. (7), $N_{V,total}$ is the total number of vanadium atoms detected, $N_{V,precip}$ is the number of vanadium atoms in precipitates and $N_{V,\alpha\text{-}Fe}$ is the calculated number of vanadium atoms in ferrite ($N_{V,total}$-$N_{V,precip}$). The fraction of vanadium in solid solution is averaged over the tips of the same specimen and is presented in the last column of Table 2. The 3D-APT measurements reveal that the total fraction of solute vanadium atoms in ferrite decreases during isothermal annealing in both steels due to continuous precipitation. However, it is not completely eliminated even after 10 h of annealing in any of the steels, indicating that the maximum volume fraction of precipitates is not reached. This is in agreement with the SANS results (see Fig. 8d) and the ThermoCalc [41] predictions for the equilibrium precipitate volume fraction stated earlier.

Note that APT allows for a local precipitation analysis over an average tip volume in the order of $\sim 10^6$ nm^3 while SANS measurements are performed in large samples with dimensions $10 \times 10 \times 1$ mm^3 ($= 10^{20}$ nm^3), leading to better statistics. Additionally, the detection efficiency of the APT instrument affects the mean distance between the atoms in the reconstructed data and

Table 2
Precipitate mean Radius, R_m (nm), number density, N_p ($10^{23}m^{-3}$) and volume fraction, f_V (%), comparison between SANS and APT. The tip volume analysed by APT and the vanadium in solid solution measured in each condition are presented as well.

Steel	Holding time	R_m (nm)		N_p ($10^{23}m^{-3}$)		f_V (%)		no. of tips and total tips volume analysed by APT	$f_{vanadium,ss}$ (%) by APT
		SANS	APT	SANS	APT	SANS	APT		
LCLV	5min	1.05 ± 0.22	1.09 ± 0.03	1.90 ± 1.95	1.85 ± 0.83	0.13 ± 0.07	0.14 ± 0.07	6 tips (3.8E6 nm^3)	79 ± 9.43
	45min	1.30 ± 0.05	1.36 ± 0.07	2.10 ± 0.38	1.57 ± 0.39	0.31 ± 0.04	0.31 ± 0.04	7 tips (5.9E6 nm^3)	41 ± 4.85
	10h	1.53 ± 0.02	2.07 ± 0.15	1.20 ± 0.08	0.59 ± 0.08	0.37 ± 0.09	0.36 ± 0.05	8 tips (5.5E6 nm^3)	25 ± 1.88
HCHV	5min	1.14 ± 0.14	1.62 ± 0.17	5.60 ± 3.44	3.60 ± 0.89	0.44 ± 0.10	0.74 ± 0.05	7 tips (4.0E6 nm^3)	28 ± 4.08
	45min	1.47 ± 0.04	1.79 ± 0.14	3.88 ± 0.53	2.85 ± 0.75	0.73 ± 0.06	0.92 ± 0.04	10 tips (6.6E6 nm^3)	20 ± 2.11
	10h	1.85 ± 0.03	2.11 ± 0.08	1.86 ± 0.11	1.37 ± 0.13	0.93 ± 0.16	0.90 ± 0.04	12 tips (5.4E6 nm^3)	12 ± 0.72

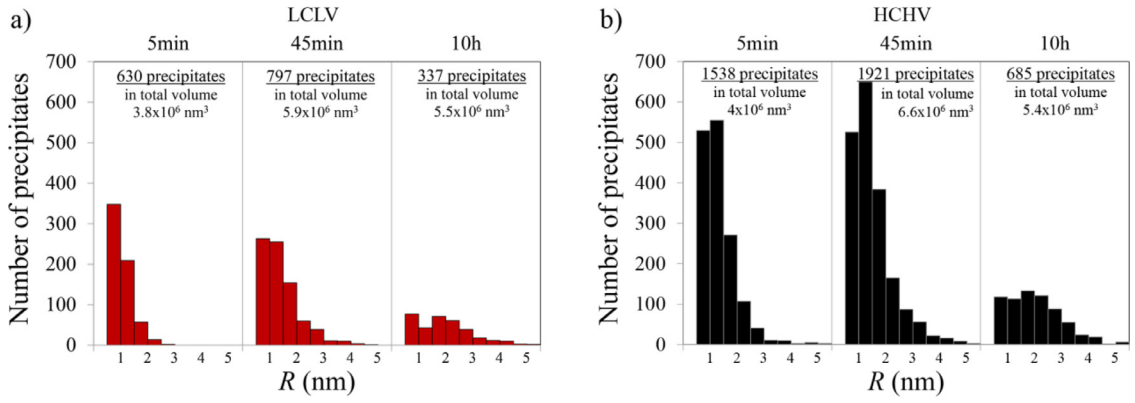

Fig. 13. Precipitate size distribution based on APT cluster analysis in a) LCLV and b) HCHV steels. The cluster analysis is performed in all the tips presented in Table 2.

consequently the results of the cluster analysis. Based on these considerations, it is reasonable to expect small deviations between the results obtained by the two techniques. Nevertheless, the good agreement between the results obtained from these two very different techniques supports the validity of our analysis.

The precipitate size distribution derived from the APT cluster analysis for the LCLV and HCHV specimens annealed for 5 min, 45 min and 10 h is plotted in Fig. 13. The total number of precipitates measured in all tips for each thermal condition is also presented. A larger number of precipitates is measured in the HCHV specimens compared to the corresponding LCLV specimens that have undergone the same heat treatment due to the higher vanadium and carbon concentration. The time evolution of the distribution is found to have the same behaviour as the one measured by SANS (Fig. 10a and b). Smaller precipitates are present in the first 5 min of annealing. As the isothermal annealing proceeds, the peak of the distribution is moving towards higher radii and the distribution broadens, indicating growth and coarsening as the dominant phenomena in these steps. Isothermal holding at 650 °C from 45 min to 10 h leads to a decrease of the total number of precipitates in both steels while coarse particles are formed. Only a few precipitates with a radius of more than 3 nm are found in both steels and the precipitate radius does not exceed 5.5 nm.

The precipitates' chemical composition profile is derived from the Proximity Diagrams (Proxigrams) [56], which are calculated based on isoconcentration surfaces (isosurfaces) of 2 at% vanadium. The evolution of the precipitates' chemical composition during annealing is presented in 1D composition profile in Fig. 14a and c for the LCLV steel and in Fig. 14b and d for the HCHV steel. A comparison is shown between the precipitate chemical composition after 5 min and 10 h of annealing in both steels. The concentration profiles are calculated in one representative precipitate for each condition. The precipitate composition evolution during annealing shows the same behaviour for both steels and is dependent on the precipitate size. It is observed that the matrix/precipitate interface is not sharp (on a nm-length scale) and that there is a gradual increase of vanadium and carbon along with a decrease of Fe concentration from the surface to the precipitate core for all the annealing conditions. The smaller precipitates formed after 5 min at 650 °C are Fe-rich despite a decrease in Fe content from their surface to their core. A drop in the fraction of Fe in the core is observed in the larger precipitates observed after 10 h and the core consists only of vanadium and carbon atoms in a stoichiometric ratio. Our results suggest no manganese enrichment in either the interphase or the randomly distributed precipitates, which is in agreement with ref. [13,19,26,27], but in contrast to Ref. [25], in which manganese enrichment was observed only in the interphase precipitates and not in the randomly distributed ones.

3.2.5. Precipitate growth / coarsening at 650 °C

The average growth of the precipitate after the austenite/ferrite transformation front has passed can be described by the model developed by Öhlund et al. [21], in which the growth is controlled by volume diffusion of atoms, i.e. in our case of vanadium atoms. During precipitate growth, the diffusion field is assumed to have a linear concentration profile with length, L, which can be calculated by [21]:

$$L = \left\{ \frac{1}{3}\left(44 + 54B + 6\sqrt{54 + 132B + 81B^2}\right)^{1/3} - \frac{2}{3\left(44 + 54B + 6\sqrt{54 + 132B + 81B^2}\right)^{1/3}} - \frac{4}{3} \right\} R, \quad (8)$$

where R is the precipitate radius and $B = (c_0^m - c_{equil}^{VC})/(c_{equil}^m - c_0^m)$. c_0^m is the concentration of vanadium in the matrix obtained from the nominal steel composition. c_{equil}^m and c_{equil}^{VC} are the equilibrium concentrations of vanadium atoms in the matrix and in the vanadium carbide precipitates, respectively, and both quantities can be derived from ThermoCalc [41]. For the LCLV steel these are $c_{equil}^m = 0.011$ wt.% and $c_{equil}^{VC} = 68$ wt.%, while for the HCHV steel $c_{equil}^m = 0.014$ wt.% and $c_{equil}^{VC} = 70$ wt.%. According to ThermoCalc [41], the c_{equil}^{VC} is slightly different between the 2 alloys and also deviates from the theoretical calculated value for pure

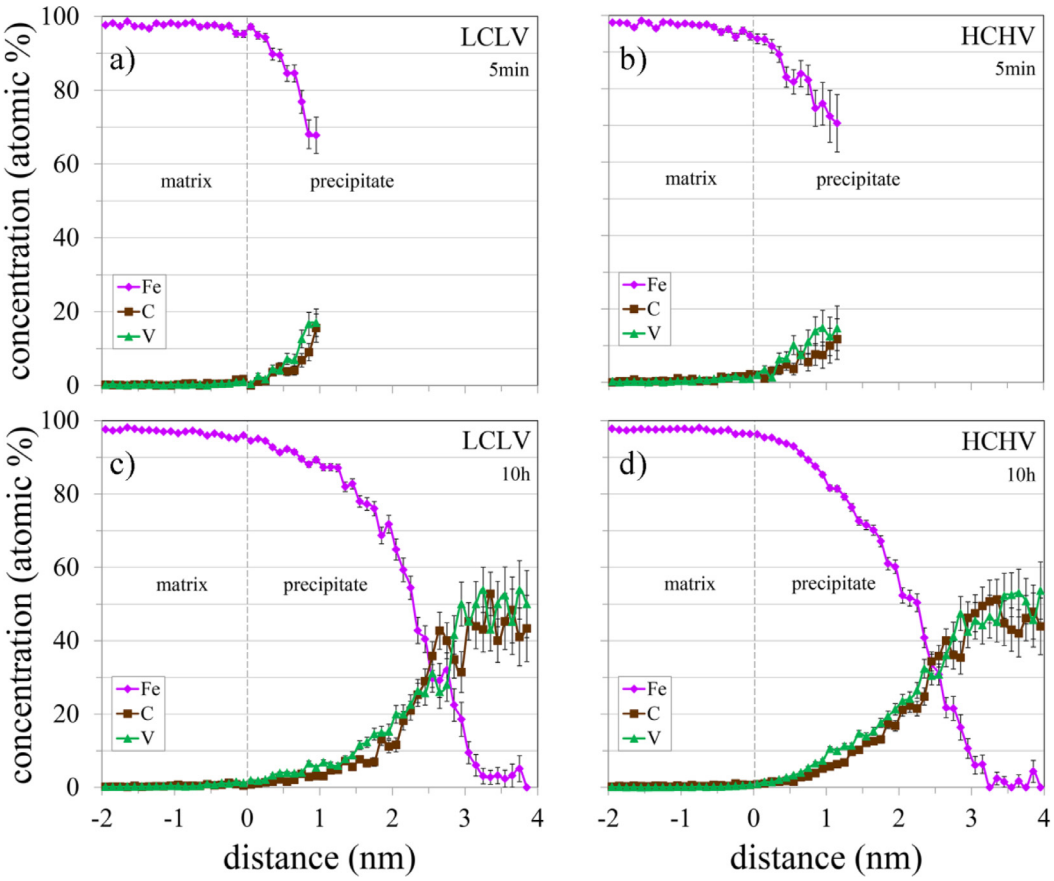

Fig. 14. Proxigrams showing the precipitate chemical composition evolution during isothermal holding at 650 °C. Specimen of a) LCLV steel annealed for 5 min, b) HCHV steel annealed for 5 min, c) LCLV steel annealed for 10 h and d) HCHV steel annealed for 10 h. They are based on isoconcentration surfaces of 2at%V and belong to one representative precipitate of this condition.

Table 3
Overlap of the diffusion fields of the VC precipitates.

Steel	Holding time	R_m (nm) by SANS	L (nm)	$d = N_p^{-1/3}$ (nm)	Overlap of diffusion fields $2R_m + 2L > d$
LCLV	20min	1.20	10.3	14.6	Yes
	45min	1.24	10.6	15.7	Yes
	2h	1.35	11.6	16.8	Yes
	10h	1.53	13.2	20.3	Yes
HCHV	20min	1.29	8.5	11.9	Yes
	45min	1.48	9.8	13.9	Yes
	2h	1.58	10.4	14.4	Yes
	10h	1.80	11.9	16.8	Yes

VC of 1:1 stoichiometric ratio, i.e. $c_{theoretical,\mathrm{equil}}{}^{VC}$ = atomic mass of vanadium / (atomic mass of vanadium + atomic mass of carbon) = 50.9/62.9 = 81%. This indicates that possibly a small amount of Fe is included in the precipitates. In particular, ThermoCalc [41] predicts a precipitate equilibrium composition of 45mol%V, 47mol%C and 8mol%Fe in both steels.

Coarsening is possible only when the diffusion fields of neighboring precipitates overlap. The length of the linear concentration profile, L, is calculated for both steels for the specimens annealed for times longer than 20 min, using the experimental mean radius values, R_m, derived by SANS. The average distance between two randomly distributed precipitates, d, is obtained by using the experimental number density values from SANS measurements and is equal to $N_p{}^{-1/3}$. For the case of the growth of spherical precipitates of the same size, the diffusion fields overlap when $2R+2L>d$. This criterion is fulfilled for both steels for all the samples annealed for longer than 20 min at 650 °C and the results are summarized in Table 3. Combining the fact that the diffusion fields overlap with the experimental observations that the precipitate number density decreases (Fig. 8b), the volume fraction increases (Fig. 8c), and the amount of vanadium in solid solution decreases (Fig. 8d) with time, proves that the observed increase in average precipitate radius (Fig. 8a) after 20 min of annealing is the result of both growth with soft impingement (overlapping diffusion fields) and coarsening.

4. Conclusions

The vanadium carbide precipitation kinetics and the austenite-to-ferrite phase transformation kinetics are studied in two vanadium micro-alloyed steels, which are isothermally heat treated at different temperatures for various holding times, by combining dilatometry, SANS, TEM and 3D-APT measurements. The conclusions are summarized as follows:

(1) Thermodynamic equilibrium calculations predict that vanadium carbide precipitates are present at 900, 750 and 650 °C. However, experiments show that neither precipitation nor phase transformation takes place in both steels when isothermally treated at 900 and 750 °C for holding times up to 10 h (except for the formation of a small fraction of ferrite at 750 °C in the LCLV steel).
(2) Experiments at 650 °C show that precipitation of vanadium carbides does take place after the onset of the austenite-to-ferrite phase transformation. This indicates that

the austenite-to-ferrite phase transformation initiates the vanadium carbide precipitation. Nucleation and growth are dominant during the first 20 min, while later precipitate growth with soft impingement (overlapping diffusion fields) and coarsening take place. The steel with two times higher vanadium and carbon concentrations (HCHV) exhibits about two times higher volume fraction and number density of the precipitates after 10 h of annealing.

(3) After 10 h of annealing at 650 °C there is still some vanadium in solid solution in both steels and the precipitate volume fraction has not reached the maximum theoretical value corresponding to thermodynamic equilibrium.

(4) Spherical (and slightly ellipsoidal) precipitates that are ordered in rows as a result of interphase precipitation as well as randomly distributed precipitates are observed by TEM and APT. The precipitate chemical composition evolution during annealing is strongly correlated to their size. The smaller vanadium carbide precipitates detected for shorter holding times are Fe-rich. The larger precipitates in the later stages of annealing are Fe-rich near the matrix/precipitate interface, but are composed of vanadium and carbon in a stoichiometric ratio of 1:1 in the core of the precipitate, with possibly a small amount of Fe, consistent with the Thermo-Calc calculations.

Overall, our findings provide quantitative information focused on the *kinetics* of the vanadium carbides in low-Carbon steels, on its *interaction* with austenite-to-ferrite phase transformation and on the *evolution of the precipitate chemical composition* during annealing at 650 °C. The acquired quantitative results can be used as input parameters for modeling the precipitation kinetics in vanadium micro-alloyed steels, which may lead to improved steel design and performance for automotive applications.

Declaration of Competing Interest

The authors declare that they have no known competing financial interests or personal relationships that could have appeared to influence the work reported in this paper.

Acknowledgements

This research was carried out under project number S41.5.14548 in the framework of the Partnership Program of the Materials innovation institute M2i (www.m2i.nl) and the Technology Foundation TTW (www.stw.nl), which is part of the Netherlands Organization for Scientific Research (www.nwo.nl). The authors wish to acknowledge the use of the Larmor beamline at ISIS (experiment number RB1669000) [57]. The experiments at ISIS pulsed neutron and muon source were supported by beam-time allocation from the Netherlands Organization for Scientific Research (NWO) through the project 721.012.102 (LARMOR). The authors are grateful to Tata Steel for providing the materials for the experiments and would like to thank N. Geerlofs (TU Delft) for his assistance to the dilatometry treatments.

Supplementary material

Supplementary material associated with this article can be found, in the online version, at doi:10.1016/j.actamat.2019.09.046.

References

[1] European Commission, A resource-efficient Europe – Flagship initiative under the Europe 2020 strategy, COM (2011) 21.
[2] Regulation EU No 333/2014, Amending Regulation (EC) No 443/2009 to define the modalities for reaching the 2020 target to reduce CO2-emissions from new passenger cars, 11 March 2014.
[3] K. Seto, Y. Funakawa, and S. Kaneko, Hot rolled high strength steels for suspension and chassis parts "NanoHiten" and "BHT" steel, JFE Technical Report, No. 10, (2007).
[4] A. Rijkenberg, A. Blowey, P. Bellina, C. Wooffindin, Advanced high stretch-flange formability steels for chassis & suspension applications, in: Proceedings of the 4th International Conference on Steels in Cars and Trucks (SCT2014), Braunschweig (Germany), 2014, p. 426.
[5] Y. Funakawa, T. Shiozaki, K. Tomita, T. Yamamoto, E. Maeda, Development of high strength hot-rolled sheet steel consisting of ferrite and nanometer-sized carbides, ISIJ Int. 44 (11) (2004) 1945–1951.
[6] T.N. Baker, Microalloyed steels, Ironmak. Steelmak. 43 (4) (2016) 264–307.
[7] WO2013167572 (A1), "Automotive Chassis Part Made from High Strength Formable Hot Rolled Steel Sheet", Tata Steel Europe.
[8] WO2014122215 (A1), A High-Strength Hot-Rolled Steel Strip Or Sheet With Excellent Formability and Fatigue Performance and a Method of Manufacturing Said Steel Strip Or Sheet, Tata Steel Europe.
[9] EP1338665 (A1), High Tensile Hot Rolled Steel Sheet and Method For Production Thereof, JFE Steel Corporation.
[10] European Commission, Report on critical raw materials for the EU, Report of the Ad hoc Working Group on defining critical raw materials, May 2014.
[11] W.B. Lee, S.G. Hong, C.G. Park, K.H. Kim, S.H. Park, Influence of mo on precipitation hardening in hot rolled hsla steels containing nb, Scr. Mater. 43 (2000) 319–324.
[12] H.-W. Yen, P.-Y. Chen, C.-Y. Hunag, J.-R. Yang, Interphase precipitation of nanometer-sized carbides in a titanium-molybdenum-bearing low-carbon steel, Acta Mater 59 (2011) 6264–6274.
[13] P. Gong, X.G. Liu, A. Rijkenberg, W.M. Rainforth, The effect of molybdenum on interphase precipitation and microstructures in microalloyed steels containing titanium and vanadium, Acta Mater 161 (2018) 374–387.
[14] S. Dhara, R.K.W. Marceau, K. Wood, T. Dorina, I.B. Timokhina, P.D. Hodgson, Precipitation and clustering in a Ti-Mo steel investigated using atom probe tomography and small-angle neutron scattering, Mat. Sci. Eng. A 718 (2018) 74–86.
[15] R. Lagneborg, T. Siwecki, S. Zajac, B. Hutchinson, The role of vanadium in microalloyed steels, Scand. J. Metall. 28 (5) (1999) 186–241.
[16] T.N. Baker, Processes, microstructure and properties of vanadium microalloyed steels, Mater. Sci. Tech. 25 (9) (2009) 1083–1107.
[17] M.-Y. Chen, M. Goune, M. Verdier, Y. Brechet, J.-R. Yang, Interphase precipitation in vanadium-alloyed steels: strengthening contribution and morphological variability with austenite to ferrite transformation, Acta Mater. 64 (2014) 78–92.
[18] G. Miyamoto, R. Hori, B. Poorganji, T. Furuhara, Interphase precipitation of vc and resultant hardening in V-added medium carbon steels, ISIJ Int. 51 (10) (2011) 1733–1739.
[19] Y.-J. Zhang, G. Miyamoto, K. Shinbo, T. Furuhara, T. Ohmura, T. Suzuki, K. Tsuzaki, Effects of transformation temperature on vc interphase precipitation and resultant hardness in low-carbon steels, Acta Mater. 84 (2015) 375–384.
[20] Y.Q. Wang, S.J. Clark, V. Janik, R.K. Heenan, D. Alba Venero, K. Yan, D.G. Mc Cartney, S. Sridhar, P.D. Lee, Investigating nano-precipitation in a V-containing HSLA steel using small angle neutron scattering, Acta Mater. 145 (2018) 84–96.
[21] C.E.I.C. Öhlund, J. Weidow, M. Thuvander, S.E. Offerman, Effect of Ti on evolution of microstructure and hardness of martensitic fe–c–mn steel during tempering, ISIJ Intern. 54 (12) (2014) 2890–2899.
[22] N.H. van Dijk, S.E. Offerman, W.G. Bouwman, M.Th. Rekveldt, J. Sietsma, S. van der zwaag, A. Bodin, R.K. Heenan, High temperature sans experiments on Nb(c,n) and MnS precipitates in HSLA steel, Metall. Mater. Trans. A 33 (2002) 1883–1891.
[23] C. Ioannidou, Z. Arechabaleta, A. Rijkenberg, R.M. Dalgliesh, A.A. van Well, S.E. Offerman, VC-precipitation kinetics studied by small-angle neutron scattering in nano-steels, Mater. Sci. Forum 941 (2018) 236–244.
[24] Y. Oba, S. Koppoju, M. Ohnuma, T. Murakami, H. Hatano, K. Sasakawa, A. Kitahara, J. Suzuki, Quantitative analysis of precipitate in vanadium-microalloyed medium carbon steels using small-angle X-ray and neutron scattering methods, ISIJ Int. 51 (11) (2011) 1852–1858.
[25] M. Nöhrer, S. Zamberger, S. Primig, H. Leitner, Atom probe study of vanadium interphase precipitates and randomly distributed vanadium precipitates in ferrite, Micron 54-55 (2013) 57–64.
[26] Y.-J. Zhang, G. Miyamoto, K. Shinbo, T. Furuhara, Quantitative measurements of phase equilibria at migrating α/γ interface and dispersion of VC interphase precipitates: evaluation of driving force for interphase precipitation, Acta Mater. 128 (2017) 166–175.
[27] Y.S. Shanmugam, M. Tanniru, R.D.K. Misra, D. Panda, S. Jansto, Microalloyed V–Nb–Ti and v steels part 2, precipitation behavior during processing of structural beams, Mater. Sci. Tech. 21 (2) (2005) 165–177.
[28] T. Epicier, D. Acevedo, M. Perez, Crystallographic structure of vanadium carbide precipitates in a model Fe-C-V steel, Philos. Mag. 88 (1) (2007) 31–45.
[29] N. Kamikawa, K. Sato, G. Miyamoto, M. Murayama, N. Sekido, K. Tsuzakie, T. Furuhara, Stress–strain behavior of ferrite and bainite with nano-precipitation in low carbon steels, Acta Mater. 83 (2015) 383–396.
[30] R.G. Baker, J. Nutting, in: Precipitation Processes in Steels, The Iron and Steel Institute, London, 1959, pp. 1–22. Special report no. 64.
[31] Y.-J. Zhang, G. Miyamoto, K. Shinbob, T. Furuhara, Effects of α/γ orientation relationship on VC interphase precipitation in low-carbon steels, Scr. Mater. 69 (2013) 17–20.

[32] G. Miyamoto, R. Hori, B. Poorganji, T. Furuhara, Crystallographic analysis of proeutectoid ferrite/austenite interface and interphase precipitation of vanadium carbide in medium-carbon steel, Metall. Mater. Trans. A 44A (2013) 3436–3443.
[33] S. Jiang, H. Wang, Y. Wu, X. Liu, H. Chen, M. Yao, B. Gault, D. Ponge, D. Raabe, A. Hirata, M. Chen, Y. Wang, Z. Lu, Ultrastrong steel via minimal lattice misfit and high-density nanoprecipitation, Nature 544 (2017) 460–464.
[34] E.A. Marquis, J.M. Hyde, Applications of atom-probe tomography to the characterization of solute behaviours, Mater. Sci. Eng. R 69 (2010) 37–62.
[35] Wiedenmann, Small angle scattering investigations of magnetic nanostructures, in: T. Chatterji (Ed.), Neutron Scattering from Magnetic Materials, Elsevier, 2006, pp. 473–519.
[36] F. Perrard, A. Deschamps, F. Bley, P. Donnadieua, P. Maugis, A small-angle neutron scattering study of fine-scale NbC precipitation kinetics in the a-Fe–Nb–C system, J. Appl. Cryst. 39 (2006) 473–482.
[37] S.M. He, N.H. van Dijk, M. Paladugu, H. Schut, J. Kohlbrecher, F.D. Tichelaar, S. van der Zwaag, In situ determination of aging precipitation in deformed Fe-Cu and Fe-Cu-B-N alloys by time-resolved small-angle neutron scattering, Phys. Rev. B 82 (2010) 174111 1-14.
[38] S. Zhang, J. Kohlbrecher, F.D. Tichelaar, G. Langelaan, E. Bruck, S. van der Zwaag, N.H. van Dijk, Defect-induced au precipitation in Fe–Au and Fe–Au–B–N alloys studied by in situ small-angle neutron scattering, Acta Mater. 61 (2013) 7009–7019.
[39] T.H. Simma, L. Sunb, D.R. Galvina, E.P. Gilbertc, D. Alba Venerof, Y. Lia, T.L. Martine, P.A.J. Bagote, M.P. Moodye, P. Hilld, H.K.D.H. Bhadeshia, S. Biroscaa, M.J. Rawsond, K.M. Perkins, A sans and apt study of precipitate evolution and strengthening in a maraging steel, Mater. Sci. Eng. A 702 (2017) 414–424.
[40] B.S. Seong, E. Shin, S. Choi, Y. Choi, Y.S. Han, K.H. Lee, Y. Tomota, Quantitative analysis of fine nano-sized precipitates in low-carbon steels by small angle neutron scattering, Appl. Phys. A 99 (2010) 613–620.
[41] J.O. Andersson, T. Helander, L. Höglund, P.F. Shi, B. Sundman, Thermo-Calc and dictra, Comp. Tools Mater. Sci. Calphad 26 (2002) 273–312.
[42] C.A. Schneider, W.S. Rasband, K.W. Eliceiri, NIH image to imagej: 25 years of image analysis, Nat. Methods 9 (7) (2012) 671–675 PMID 22930834 (on Google Scholar).
[43] O. Arnold, J.C. Bilheux, J.M. Borreguero, A. Buts, S.I. Campbell, L. Chapon, M. Doucet, N. Draper, R. Ferraz Leal, M.A. Gigg, V.E. Lynch, A. Markvardsen, D.J. Mikkelson, R.L. Mikkelson, R. Miller, K. Palmen, P. Parker, G. Passos, T.G. Perring, P.F. Peterson, S. Renc, M.A. Reuter, A.T. Savici, J.W. Taylor, R.J. Taylor, R. Tolchenov, W. Zhou, J. Zikovsky, Mantid-Data analysis and visualization package for neutron scattering and μ sr experiments, Nuc. Inst. Meth. Phys. Res. A 764 (2014) 156–166.
[44] D.J. Larson, D.T. Foord, A.K. Petford-Long, T.C. Anthony, I.M. Rozdilsky, A. Cerezo, G.W.D. Smith, Focused ion-beam milling for field-ion specimen preparation: preliminary investigations, Ultramicroscopy 75 (1998) 147–159.
[45] R. Córdoba, N. Sharma, S. Kölling, P.M. Koenraad, B. Koopmans, High-purity 3D nano-objects grown by focused-electron-beam induced deposition, Nanotechnology 27 (2016) 355301.
[46] B. Gault, F. Danoix, K. Hoummada, D. Mangelinck, H. Leitner, Impact of directional walk on atom probe microanalysis, Ultramicroscopy 113 (2012) 182–191.
[47] M. Thuvander, J. Weidow, J. Angseryd, L.K. Falk, M. Sonestedt, K. Stiller, H.O. Andrén, Quantitative atom probe analysis of carbides, Ultramicroscopy 111 (2011) 604.
[48] M. Enemoto, N. Nojiri, Y. Sato, Effects of vanadium and niobium on the nucleation kinetics of proeutectoid ferrite at austenite grain boundaries in Fe-C and Fe-C-Mn alloys, Mater. Trans. JIM 35 (12) (1994) 859–867.
[49] M.J. Peet, H.K.D.H. Bhadeshia : mucg83. (University of Cambridge, 2006), http://www.msm.cam.ac.uk/map/steel/programs/mucg83.html.
[50] T. Narayanan, Synchrotron small-angle X-Ray scattering, in: R. Borsali, R. Pecora (Eds.), Soft-Matter Characterization, Springer, 2008, pp. 899–948.
[51] L.A. Feigin, Structure Analysis by Small-Angle X-ray and Neutron Scattering, New York, 1987.
[52] M. Perez, Gibbs–Thomson effects in phase transformations, Scripta Materialia 52 (2005) 709–712.
[53] Q. Yong, X. Sun, Z. Li, Z. Wang, K. Zhang, Physical metallurgical principles of titanium microalloyed steel-dissolution and precipitation of titanium-bearing secondary phases, in: X. Mao (Ed.), Titanium Microalloyed Steel: Fundamentals, Technology, and Products, Springer, 2019, p. 94.
[54] G.G. Long, L.E. Levine, Ultra-small-angle X-ray scattering from dislocation structures, Acta Crystallogr. A61 (2005) 557–567.
[55] D. Vaumousse, A. Cerezo, P.J. Warren, A procedure for quantification of precipitate microstructures from three-dimensional atom probe data, Ultramicroscopy 95 (2003) 215–221.
[56] O.C. Hellman, J.A. Vandenbroucke, J. Rusing, D. Isheim, D.N. Seidman, Analysis of three-dimensional atom-probe data by the proximity histogram, Microsc. Microanal. 6 (2000) 437–444.
[57] A.A. van Well, R.M. Dalgliesh, S.E. Offerman, C. Ioannidou and Z. Arechabaleta Guenechea, (2016): 1669000, STFC ISIS Facility, doi:10.5286/ISIS.E.83552069.